

Programmable Switching of Molecular Transitions via Plasmonic Toroidal Nanoantennae

Arda Gulucu^{1,2} and Emre Ozan Polat^{1,2,*}

¹*Department of Physics, Bilkent University, 06800, Ankara, Turkey*

²*UNAM - National Nanotechnology Research Center and Institute of Materials Science and Nanotechnology, Bilkent University, 06800, Ankara, Turkey*

**Corresponding author: emre.polat@bilkent.edu.tr*

Abstract

The ability to switch and program molecular transitions via deterministically located plasmonic nanoantennae presents opportunities for wide spectrum of applications from biosensors to quantum computing. Due to its topology, toroidal nanoantenna (TNA) focuses immense amount of three-dimensional (3D) local electric field by toroidal moment while allowing pre and post positioning around quantum emitters (QEs). Here, we report complete switching of molecular transition energies of quantum objects (QOs) with modulation depth of 99.9% over 2840-fold radiative enhancement. At optimized TNA geometries, Fano interference between the broadband plasmonic continuum and narrow quantum transitions of QOs suppresses both radiative and non-radiative decay channels near 850 nm, yielding an observable full switching that traps energy within the hybrid mode instead of re-emitting it. To show the promises of the concept, we further demonstrate systems with multiple QOs where spectral degeneracy enhances the transparency bandwidth, while detuning generates distinct minima, enabling individually addressable spectral responses. These results establish plasmonic TNA as a promising architecture for spectral detection of single or multi-molecule configurations with high sensitivity and empowers the user for the implementation of quantum mode switches to be used in photonic processing.

Keywords: Toroidal nanoantenna, Fano interference, Purcell enhancement, Quantum emitter, Plasmonic mode switching

Introduction

Plasmonics exploits the collective oscillations of free electrons at metal-dielectric interfaces to concentrate electromagnetic energy into nanoscale volumes known as “hotspots” [1,2]. Localized surface plasmon resonances (LSPRs) in metallic nanoparticles generate intense electric fields near their surfaces, enabling surface-enhanced Raman scattering, fluorescence modulation, and nanoscale sensing [3–6]. Spherical and rod-shaped nanoparticles have been extensively studied in the context of field localization [7–9]. Unlike commonly used spheres, rods or rings, TNA supports closed poloidal displacement currents that realize a toroidal (anapole) moment, squeezing fields into the inner rim with small mode volume [10,11]. Offering unique confinement properties, the topology of a metallic TNA produces a 3D hotspot volume with simultaneous radial and axial localization, supported by circulating plasmon modes [12–16]. This configuration provides versatile tunability of resonance wavelength through its aspect ratio while delivering a high local density of optical states (Purcell enhancement [17]) and multipolar mode mixing [18]. These features make toroidal plasmonic resonators a strong contender for engineering strong light–matter interactions at deterministic emitter locations.

When a narrow discrete resonance interacts coherently with a broad plasmonic continuum, their interference gives rise to an asymmetric Fano lineshape, manifested as a sharp dip or transparency window within the otherwise broad scattering spectrum [19,20]. The discrete state can originate from QOs such as molecules, quantum dots, or excitons possessing intrinsically narrow linewidths [21–26]. These hybrid plasmon-QO Fano resonances produce spectrally sharp and tunable features with enhanced local fields and strong dispersion enabling promising results in high-sensitivity sensing, optical switching, low-threshold lasing, and nonlinear photonic functionalities [27,28].

Here, we introduce an active mode-switching mechanism for a quantum emitter (QE) coupled to a toroidal nanoantenna (TNA), enabling discrete quantum modes to be selectively controlled across a strongly enhanced photoluminescence (PL) spectrum. Although TNAs have attracted significant attention, prior work has largely remained within the framework of passive resonance engineering. In emitter-coupled TNAs, earlier studies mainly focused on Purcell enhancement, radiation efficiency, and emission directivity [14]. Similarly, finite-element studies comparing single-torus and dimer geometries quantified linewidth, near-field enhancement, and Purcell factors [29], but did not address whether a radiatively optimized TNA could be transformed into an actively programmable interference platform.

More importantly, previous plasmon-exciton Fano studies demonstrated spectral modulation but did not achieve complete switching of the emission channel [30–33], while Fano/metasurface implementations generally relied on complex multi-resonator unit cells or three-dimensional metamaterial architectures [34–38]. In contrast, we show that a single molecule, described by a Lorentzian dielectric response and tuned into resonance with the QE

emission, can completely suppress the radiative and non-radiative decay channels that are otherwise enhanced by factors of 2840 and 1056, respectively, in the vicinity of the TNA.

The key novelty is that the molecule does not need to act as a bright emitter itself; instead, it switches the TNA-enhanced decay pathways by sharply perturbing the local electromagnetic response through the frequency-dependent complex polarizability, $\epsilon(\omega)$. This makes the concept broadly applicable as a general and programmable platform for emission control in toroidal plasmonic systems, with potential relevance to defect centers, molecules, quantum dots, and other quantum objects possessing intrinsically narrow linewidths.

The strict control of the quantum mode switches is provided through the toroid's aspect ratio that optimizes the local density of optical states (LDOS) thereby yields spectral enhancement. Interference of a closely located QO induces a Fano transparency in the enhanced spectrum, yielding a complete switching of quantum modes over the plasmonic continuum. Our approach is based on the specific regime of TNA aspect ratios, that provides a large span of emitter-antenna distances where the QE radiative decay rate dominates over non-radiative counterpart. Presented numerical study simulates the hybrid system consisting of QOs, TNAs and QEs through finite-difference time domain (FDTD) simulations and reports a framework of crucial cases for the practical applications. The experimental implementation of the approach is viable through various fabrication methods provided that the toroidal structures can be fabricated around QEs, and the QOs can be imposed later. Alternately, the TNA can be located around a defect center, ensuring deterministic alignment.

To show the promises of our approach, the investigation is extended from single QO to multi-QO configurations demonstrating that spectral degeneracy enhances the transparency bandwidth, while detuning among multiple QO (such as the Stark effect [39]) generates multiple minima that are individually addressable over the plasmonic continuum. The reported results provide a benchmark for spectral sensing and manipulation of quantum states thus, we anticipate that the efficient quantum mode switching would yield applications where the related wavelength needs to be selectively sensed (or blocked) such as super resolution bioimaging [40], quantum sensing [41], programmable photonic circuits [42] and future display technologies [43].

Results

We first consider a system composed of a dipolar quantum emitter (QE) placed at a distance d from a silver toroidal nanoantenna (TNA) characterized by major radius R and cross-sectional radius α (**Figure 1a**). **Figure 1b** presents a snapshot of the electric-field intensity distribution at $t \approx 0.14\text{ps}$, showing that the dipole field emitted by the QE becomes strongly localized around the TNA. By varying the aspect ratio α/R , the plasmonic resonance wavelength λ_{res} of

the TNA can be systematically tuned. For a fixed total outer size of $R + \alpha = 60$ nm, increasing α/R from 0.1 to 1 shifts λ_{res} from the near-infrared to the UV-visible region (Figure 1c), demonstrating that the same TNA platform can be adapted to a broad range of QE transition energies. Consistent with analytical expectations, decreasing the aspect ratio reduces the effective toroidal volume and produces a red shift in the resonance wavelength [12]. In contrast, as α/R approaches unity, the toroid increasingly resembles a metallic nanosphere of radius $R + \alpha$, causing λ_{res} to saturate for $\alpha/R \gtrsim 0.7$ (Figure 1c).

Figure 1d shows the normalized radiative and non-radiative decay rates for an emitter-antenna separation of $d = 3$ nm and a fixed total radius $R + \alpha = 60$ nm. Although non-radiative decay is often expected to dominate at such short distances because of near-field energy transfer to the metal, we identify a counterintuitive regime in which the radiative decay channel exceeds the non-radiative one. In particular, the radiative rate reaches its maximum near $\alpha/R = 0.2$, and remains larger than the non-radiative contribution over the range $0.2 \lesssim \alpha/R \lesssim 0.6$, as highlighted in the inset of **Figure 1d**.

This intermediate regime can be understood analytically through the Purcell factor,

$$F_P = \frac{\gamma_{\text{tot}}}{\gamma_0} = \frac{3}{4\pi^2} \left(\frac{\lambda}{n}\right)^3 \frac{Q}{V_{\text{eff}}}, \quad (1)$$

where $\gamma_{\text{tot}} = \gamma_r + \gamma_{nr}$ is the total decay rate of the emitter in the presence of the nanoantenna, γ_0 is the free-space decay rate, λ is the wavelength, n is the refractive index of the surrounding medium, Q is the quality factor, and V_{eff} is the effective mode volume. Decreasing the aspect ratio produces two concurrent effects: it redshifts the resonance to longer wavelengths and reduces the effective mode volume. Together, these changes increase the LDOS and thus enhance the Purcell factor, while the accompanying reduction in Q remains comparatively minor.

Within the optimal range, $0.2 \leq \alpha/R \leq 0.6$, the LDOS enhancement couples predominantly to radiative channels, so the plasmonic TNA effectively operates as a cavity despite its modest quality factor. For smaller aspect ratios, $\alpha/R < 0.2$, the system enters a Rayleigh-like absorption regime in which losses dominate. For larger aspect ratios, $\alpha/R > 0.6$, the response gradually transitions toward that of a silver nanosphere, where Ohmic dissipation becomes dominant. The sharp increase in non-radiative decay beyond $\alpha/R \approx 0.6$ is therefore best interpreted as a modal crossover rather than a smooth continuation of the same toroidal mode.

As shown in **Supplementary Figures S1-S3**, although a toroid-like resonance persists for $\alpha/R = 0.7-1.0$, the dominant plasmonic response shifts to a sphere-like mode near 342 nm, which is strongly non-radiative. As the inner opening of the toroid closes, the structure increasingly resembles a compact nanosphere, weakening the radiatively efficient toroidal

resonance and favoring Ohmic loss. Hence, the abrupt rise in γ_{nr} does not arise from a gradual modification of the original toroidal mode, but from the emergence of a loss-dominated sphere-like plasmon branch. The corresponding values of λ_{res} and the normalized decay rates for different aspect ratios are summarized in **Table 1**.

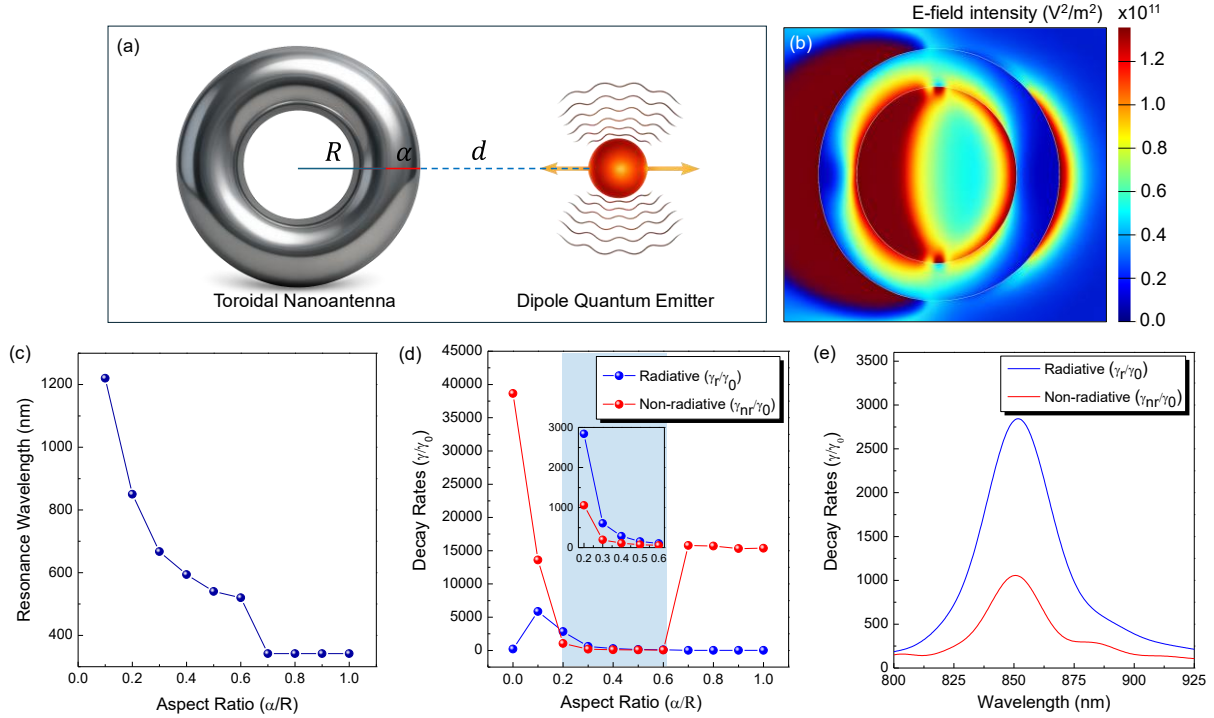


Figure 1. Geometry-controlled radiative enhancement and spectral tunability in a quantum emitter-toroidal nanoantenna system. (a) Schematic illustration of the quantum emitter-toroidal nanoantenna (QE-TNA) system for plasmonic enhancement. A dipole QE (red) located at distance d away from a silver TNA, with a major radius R and cross-section radius α . (b) Snapshot of local electric field intensity ($|E_{loc}|^2$) at $t \approx 0.14$ ps for the presented QE-TNA system. Color bar shows the E-field intensity scale. (c) Resonance wavelengths for increasing aspect ratios (α/R). By changing the ratio between 0.2 and 1, one can yield a broadband range of resonance wavelengths from NIR to UV-Vis (d) Normalized decay rate (γ/γ_0) values at resonance wavelength (850 nm) with respect to TNA aspect ratio (for $d = 3$ nm). Inset shows the intermediate aspect ratio regime where the radiative decay rates (γ_r/γ_0) overcome the non-radiative (γ_{nr}/γ_0) counterparts. (e) Decay rate spectra of QE-TNA coupling. For the optimal condition of $\alpha/R = 0.2$ the enhancement of LDOS boosts the radiative decay rate over the non-radiative counterpart around the resonance wavelength of $\lambda_{res} = 850$ nm.

Table 1. Complete parameter set for the dipole QE-TNA coupling as a function of toroidal aspect ratio. Listed are the plasmon resonance wavelength (λ_{res}), normalized radiative decay rate (γ_r/γ_0), and normalized non-radiative decay rate (γ_{nr}/γ_0) for different values of the aspect ratio (α/R). The results identify an optimal intermediate geometry for radiative enhancement and a high-aspect-ratio regime characterized by increased non-radiative loss and resonance saturation.

<i>Aspect Ratio</i> (α/R)	<i>Plasmon Resonance Wavelength</i> λ_{res} (nm)	<i>Normalized Radiative Decay Rate</i> $\gamma_r/\gamma_0 (\times 10^3)$	<i>Normalized Non-radiative Decay Rate</i> $\gamma_{nr}/\gamma_0 (\times 10^3)$
0.1	1220	5.870	13.60
0.2	850	2.840	1.056
0.3	667	0.608	0.195
0.4	600	0.284	0.109
0.5	542	0.155	0.073
0.6	514	0.104	0.056
0.7	342	0.020	15.80
0.8	342	0.015	15.70
0.9	342	0.017	15.33
1.0	342	0.013	15.38

We therefore identify $\alpha/R = 0.2$ as the optimal geometry for maximizing radiative efficiency, yielding a strongly enhanced radiative decay rate of $\gamma_r/\gamma_0 = 2840$ while keeping non-radiative losses comparatively lower at $\gamma_{nr}/\gamma_0 = 1056$, both centered around $\lambda_{res} = 850$ nm (**Figure 1e**). Although an individual quantum emitter typically possesses a narrow Lorentzian emission linewidth, the broad spectral feature observed between 800 and 900 nm in **Figure 1e** does not represent the intrinsic emission profile of the emitter. Rather, it reflects the Purcell enhancement spectrum imposed by the plasmonic environment. In other words, the TNA provides a broadband plasmonic continuum that reshapes the LDOS experienced by the emitter, and the resulting radiative and non-radiative decay spectra inherit this broadband character. This result shows that a radiatively optimized TNA can be converted from a broadband Purcell enhancer into an actively switchable Fano platform by coupling it to a single narrow-linewidth molecular resonance.

Next, we place a single molecule, modeled by a sharp Lorentzian dielectric response, at the center of the TNA (**Figure 2a**). When coupled to the broadband plasmonic continuum of the

QE-TNA system, the molecular polarization introduces a narrow spectral channel that interferes with the broad antenna response, forming a hybrid system that supports Fano-type interference between discrete and continuum states. This interference modifies the optical response of the system and generates the characteristic asymmetric Fano line shape. **Figures 2b** and **2c** show the normalized radiative and non-radiative decay spectra, respectively. In the bare QE-TNA system, both γ_r and γ_{nr} vary smoothly, consistent with conventional broadband plasmonic dissipation. However, when a QO of 20 nm radius is introduced at the center, a sharp suppression emerges near $\lambda = 850$ nm, marking the onset of the Fano transparency window. The simultaneous reduction of both decay channels indicates that destructive interference at this wavelength suppresses the LDOS and inhibits energy transfer into both radiative and dissipative pathways.

Importantly, the switching behavior is far more pronounced in the radiative channel than in the non-radiative one. The radiative decay is completely switched off, collapsing from $2840\gamma_0$ to nearly zero, whereas the non-radiative decay is reduced from $1056\gamma_0$ to $249\gamma_0$. This asymmetry reflects the fundamentally irreversible nature of material losses, which remain limited by electron-phonon and phonon-phonon dissipation even when radiative emission is fully suppressed. **Figure 2d** further confirms this interpretation through near-field intensity maps taken at resonance and off-resonance wavelengths around the transparency window. Strongly localized fields are observed around the TNA surface away from the transparency condition, whereas at $\lambda = 850$ nm the field intensity collapses dramatically due to destructive interference between the QO-induced polarization and the plasmonic continuum. This collapse directly visualizes the optical switching action of the Fano resonance and the associated suppression of the LDOS.

The overall Purcell response is summarized in **Figure 2e**, which compares the Purcell factor spectra of the bare QE-TNA system (cyan curve) and the hybrid QE-TNA-QO system (orange curve). The introduction of the narrow QO resonance transforms the smooth broadband continuum into an asymmetric spectral response with a pronounced transparency dip. This minimum corresponds to the destructive interference point, where the real part of the QO self-energy also induces a slight resonance shift from 348 THz to approximately 353 THz, consistent with the expected signature of Fano interference between discrete and continuum states [44]. Unlike previous Fano-based plasmonic implementations that often rely on complex cavity constraints or multi-resonator architectures, the present system achieves strong enhancement and near-complete radiative suppression in a compact toroidal platform. This simplicity is particularly attractive for scalable three-dimensional multipixel arrangements in which individual elements may be independently addressed.

To further clarify the physical behavior of the system and to provide a practically useful framework for experimental implementation, we next investigate the dependence on emitter-antenna separation d . The normalized decay rates are computed as a function of distance and fitted with an exponential form to capture the resonance dynamics of the hybrid structure.

Figure 3a shows the normalized radiative and non-radiative decay rates at 850 nm as a function of emitter-antenna separation in the absence of the central QO. The extracted peak values of γ_r and γ_{nr} are fitted using an exponential distance-dependent function of the form $y(d) = e^{a+bd+cd^2}$, where a , b , and c are fitting constants, consistent with previous numerical and analytical approaches (See **Methodology**) [6,45].

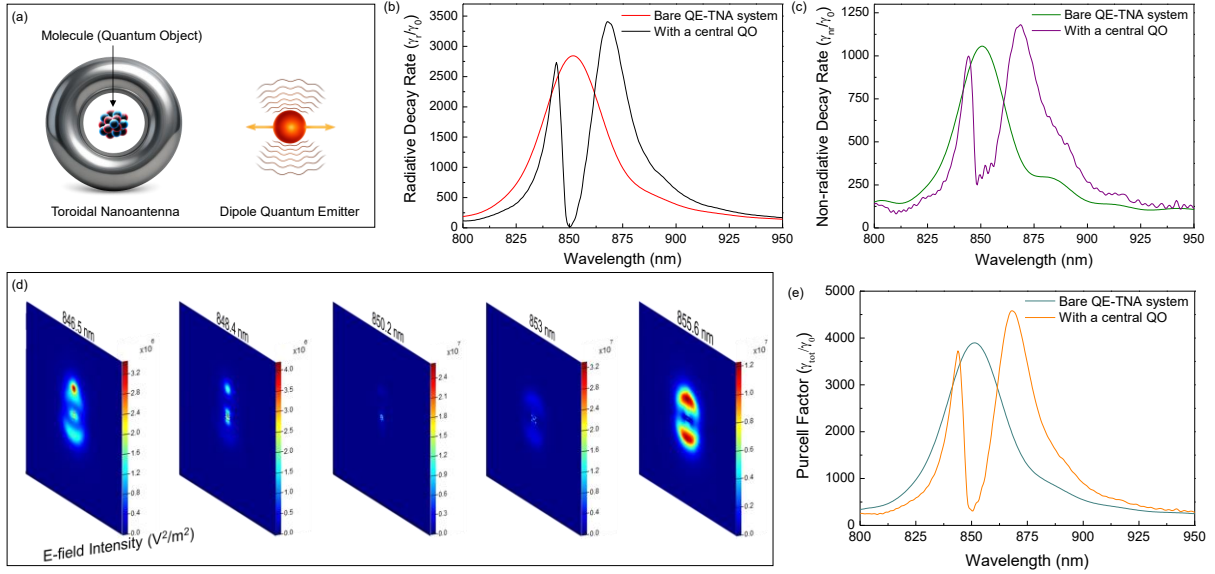


Figure 2. Active suppression of plasmon-enhanced decay through Fano interference in the QE-TNA-QO hybrid system. (a) Schematic of the hybrid system depicting the QE-TNA coupling to a central molecule (QO). The dispersive QO introduces a phase-shifted polarization that interferes with the broadband plasmonic continuum of the TNA, producing a Fano-type hybrid mode. (b) Normalized radiative decay rate (γ_r/γ_0) of the system with and without QO. (c) Normalized non-radiative decay rate of the system with and without QO. The introduction of the QO leads to a sharp suppression in both radiative and non-radiative channels around $\lambda = 850$ nm, indicating destructive interference and energy trapping within the hybrid mode. (d) Electric field intensity maps at resonant and off-resonant wavelengths around the transparency region. The collapse of near-field enhancement at the resonance and the enhancement at the off-resonance wavelengths around the transparency window are clearly visible. (e) Purcell factor spectra of the system. The emergence of a narrow transparency dip in the Purcell factor confirms the Fano interference between the discrete QO resonance and the plasmonic continuum.

For large emitter-antenna separations, $d \gg 50$ nm, both the radiative and non-radiative decay rates approach unity, indicating recovery of the free-space emission regime. As the emitter moves closer to the toroidal nanoantenna, the non-radiative decay increases gradually, whereas the radiative decay rises sharply at very small gaps, which is unusual for metal-based plasmonic

systems. Notably, the radiative channel remains dominant over the entire distance range considered. This behavior originates from the toroidal geometry and the optimized aspect ratio of the antenna, which together promote radiative local-density-of-states enhancement while suppressing the loss-dominated near-field transfer pathways that typically emerge in conventional plasmonic structures. As a result, the proposed configuration effectively avoids the usual Förster-type non-radiative quenching at sub-10-nm separations and enables access to exceptionally large enhancement factors.

Figure 3b shows the radiative decay spectra for different QE-TNA separations ($d = 3, 4, 5, 10, 15, 20, 25, 30, 40,$ and 50 nm) in the presence of the central QO. Each spectrum exhibits a characteristic Fano transparency dip near 850 nm, although the modulation depth varies with distance. As separation increases, the dipole-plasmon coupling weakens, and the destructive interference responsible for the Fano cancellation becomes progressively less pronounced. This behavior is quantified in **Figure 3c** through the transparency contrast, $\Delta I/I\%$, defined as the relative suppression of the radiative decay rate at the resonance wavelength. At $d = 3$ nm, the transparency reaches 99.9% and remains essentially unchanged up to $d = 10$ nm, thereby defining a practically useful distance window for complete switching of the radiative channel. Beyond this range, the transparency decreases only slightly, reaching 97.8% even at $d = 50$ nm. The persistence of this near-complete switching over such a wide distance range provides substantial design flexibility for experimental implementation.

We next extend the analysis beyond the single-QO case, motivated by the fact that practical implementations will generally require multiple molecular resonances. The single central molecule establishes the fundamental mechanism: Fano interference between a narrow quantum-object resonance and the broadband toroidal plasmonic continuum. Building on this basis, multiple QOs can introduce additional interfering narrow resonances and thereby enrich the spectral response. In principle, a shared plasmonic mode may also mediate emitter-emitter interactions through the electromagnetic Green's function. In the present work, however, we adopt an effective independent-response description in which each QO interacts primarily with the same toroidal plasmonic background. Accordingly, the multi-QO features discussed below are interpreted as collective spectral modulation generated by several narrow resonances interfering with a common broadband continuum, rather than as explicit plasmon-mediated entanglement. To capture this behavior, we place additional molecules within the three-dimensional hotspot region of the TNA and examine how intermolecular spacing and spectral detuning affect the resulting switching dynamics.

To extract the decay spectra and the corresponding Fano-switching behavior for single- and multiple-QO configurations, we fix the dipole QE at $d = 3$ nm and keep one molecule (QO-1) at the center of the TNA. Three additional external QOs, each with a radius of 20 nm, are then positioned around the TNA with a lateral separation of 5 nm in different directions (**Figure 4a**). When all QOs are resonant at 850 nm, we find that the Fano transparency bandwidth increases systematically with the number of coupled QOs (**Figure 4b**). While a single molecule yields a

transparency bandwidth of 14 nm, the full width at half maximum (FWHM) broadens to 22, 27, and 34 nm for 2, 3, and 4 QOs, respectively. Importantly, this broadening occurs without a significant shift in the transparency wavelength, indicating that the resonance frequency remains essentially fixed while the spectral switching window becomes wider. This behavior arises because multiple discrete resonances reinforce destructive interference within the same plasmonic continuum. A slight increase in transparency depth is also observed with increasing QO number; however, this effect remains modest because the dipole QE-TNA system is already operated under near-optimal conditions, yielding a maximum transparency of 99.9% at $d = 3$ nm for $\alpha/R = 0.2$ (See **Figure 3c** and **Table 1**).

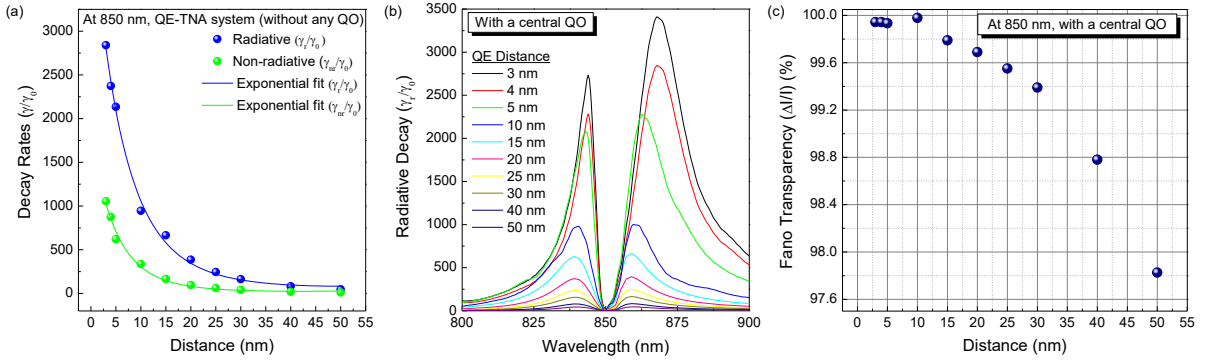


Figure 3. Distance-tolerant Fano switching enabled by the radiatively optimized toroidal nanoantenna geometry. (a) Normalized radiative and non-radiative decay rates at the QE emission wavelength (850 nm) as a function of emitter-antenna separation, in the absence of the central QO. Owing to the toroidal topology and optimized antenna geometry, the radiative decay remains higher than the non-radiative decay over the full distance range ($d = 3$ -50 nm), thereby preserving observable emission enhancement even at small separations. The exponential fits indicate convergence toward the free-space limit at large distances. (b) Radiative decay spectra for different emitter-antenna separations in the presence of the central QO. All spectra exhibit a characteristic Fano transparency dip near 850 nm, where the Lorentzian QO resonance is aligned with the QE emission. As d increases, the dipole-plasmon coupling weakens and the interference contrast gradually decreases. (c) Fano transparency contrast, expressed as the percentage suppression of the radiative decay, $\Delta I/I\%$, as a function of emitter-antenna separation. Complete switching is maintained below $d = 10$ nm, while the modulation depth decreases only slightly from 99.9% to 97.8% over the $d = 10$ -50 nm range, demonstrating a robust and practically useful switching regime.

Having established the behavior of multiple resonant QOs, we next examine the effect of spectral detuning between them. In realistic systems, perfect spectral alignment among multiple quantum objects is rarely maintained, since local environmental disorder, applied electric fields, or mechanical strain can shift their transition energies. For example, the quantum-confined

Stark effect (QCSE) is widely used to tune the emission or absorption wavelength of quantum dots and single molecules through static electric fields [46]. Similar spectral tuning can also be achieved intentionally by strain engineering, as demonstrated for quantum dots and layered-material emitters [47]. **Figure 4c** shows the radiative decay spectra for a double-QO configuration consisting of QO-1 and QO-2 under different detuning conditions. For simplicity, QO-1 is kept fixed at the resonance wavelength of 850 nm, while QO-2 is progressively detuned. We find that detuning one of the QOs produces a pronounced modification of the plasmonic continuum, generating a second transparency dip that shifts toward longer wavelengths as the detuning increases. For tuning values of 26.4, 32.8, and 48.6 meV, the second transparency window associated with QO-2 appears at 865, 870, and 880 nm, respectively, with bandwidths of approximately 10 nm.

To demonstrate the practical potential of this approach, we finally consider multiple detuned QOs distributed within the three-dimensional hotspot region of the TNA, as would be relevant for applications requiring the selective sensing or suppression of spectral signals from specific molecules. **Figure 4d** shows the spectral fingerprints of four QOs encoded as distinct transparency dips in the radiative decay spectrum of the hybrid system. When spectrally detuned QOs are positioned at fixed locations, each one generates its own Fano dip at its corresponding resonance wavelength, demonstrating that multiple spectral minima can coexist within the same plasmonic continuum. In the configuration considered here, distinct transparency dips appear at 850, 865, 870, and 880 nm for detuning values of 0, 26.4, 32.8, and 48.6 meV, respectively. This demonstrates that the toroidal plasmonic continuum can host multiple independently programmable Fano channels within a single nanoantenna platform yielding the possibility of individually addressable switching, or sensing, of molecular resonances within an ensemble.

We emphasize that complete switching of individual quantum modes is only achievable when the QOs are placed within the maximized local-field regions inside or around the TNA. Therefore, non-deterministic molecular placement may not produce pronounced spectral dips in the plasmonic continuum. In addition, an excessively large number of QOs or molecular clustering may suppress the visibility of the reported effect by perturbing the local mode structure. Taken together, these results establish the toroidal nanoantenna as a platform for individually addressable quantum-mode switching over a shared plasmonic continuum, with strong modulation depths achievable when deterministic positioning is feasible.

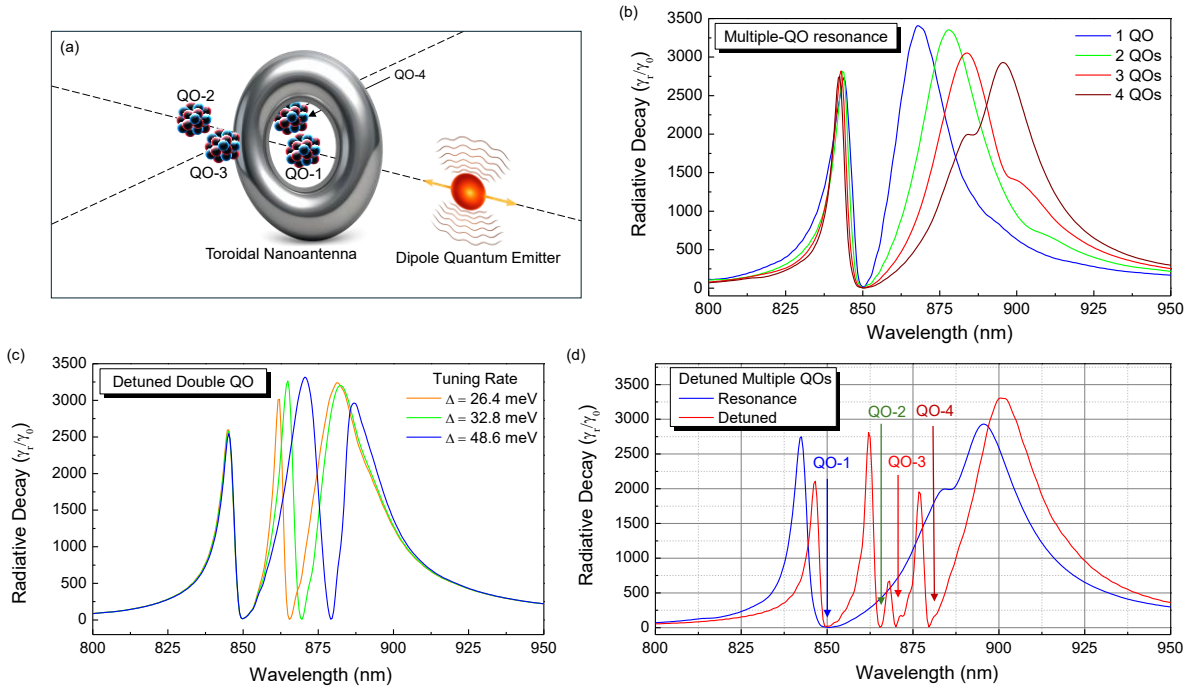


Figure 4. Individually addressable multi-molecule Fano switching in a toroidal plasmonic continuum. (a) Schematic of the multi-QO configuration, where one QO is positioned at the center of the TNA and additional QOs are placed around the outer hotspot region with fixed lateral separations. The dipolar QE remains at $d = 3$ nm from the antenna. (b) Radiative decay spectra for increasing numbers of resonant QOs. When all QOs are tuned to 850 nm, the Fano transparency progressively broadens with increasing QO number, while the transparency wavelength remains nearly unchanged. This demonstrates that multiple narrow resonances can collectively widen the switching bandwidth without substantially shifting the spectral position of the transparency window. (c) Radiative decay spectra for the double-QO configuration under spectral detuning. QO-1 is kept resonant at 850 nm, while QO-2 is progressively detuned, causing the emergence and redshift of a second transparency dip. This shows that individual molecular resonances can imprint distinct and controllable spectral signatures onto the same plasmonic continuum. (d) Radiative decay spectra for four spectrally detuned QOs placed within the three-dimensional hotspot region of the TNA. Each QO generates a separate Fano transparency dip at its corresponding resonance wavelength, demonstrating individually addressable switching of multiple quantum modes within a single toroidal plasmonic platform.

Conclusion, Discussion and Outlook

In this work, we numerically demonstrated a TNA that emulates a photonic cavity within a specific range of aspect ratios. We developed a comprehensive numerical framework to engineer Fano-resonance phenomena in a hybrid platform composed of a silver plasmonic TNA, a point dipole QE, and one or more narrow Lorentzian-dielectric QOs representing molecules. Treating each QO as a discrete narrow-band oscillator evanescently coupled to the TNA, we performed extensive FDTD simulations to:

1. Identify a pronounced Fano transparency dip at $\lambda \approx 850$ nm due to TNA topology, originating from interference between the broadband TNA plasmon continuum and the narrow QO resonance. The efficiency of the modulation depth (over $2840\gamma_0$) yields complete switching and high sensitivity for practical applications.
2. Demonstrate that the Fano-dip transparency reaches a complete transparency (99.9%) for optimal emitter–antenna separations, and TNA provides a large span of distances ($d = 3\text{-}50$ nm) for design freedom in experimental implementations.
3. Introduce multiple QOs within the 3D hotspot region of TNA that broadens the Fano dip when QOs are spectrally resonant and leads to distinct transparency minima when they are spectrally detuned.

Experimental implementation of the presented concept can be realized by coupling a silver TNA to a narrow-line quantum emitter operating in the near-infrared, such as the V1 silicon-vacancy center in 4H-SiC (≈ 861 nm) or a defect center in hBN (550-850 nm band), and probing the predicted Fano-assisted modulation of the emitter’s decay rate using a co-localized fluorescent dipole tuned to the same spectral window near 850 nm [48–50]. To that end, we demonstrated an interval that the toroidal geometry remains active for (aspect ratio regime from 0.2 to 0.6), broadband operation with the fabrication of various TNA geometries.

While extending this design into arrays may offer a powerful route toward multifunctional photonic metasurfaces [51], the proposed hybrid system, exhibiting sharp, high-contrast Fano transparency dips in the radiative decay spectrum, is well suited for label-free, real-time biomolecular sensing at the single-molecule level [52]. Moreover, exploiting the presented single and multiple dip concepts within a lithographically compatible toroidal geometry, promises applications in lab-on-chip biosensors with sub-picomolar sensitivity [53]. reconfigurable dual-band filters, slow-light elements for integrated photonics [54,55] and voltage-gated fluorescence switching or dual-colour spacer cavities for quantum-photonic and bio-imaging technologies [56,57]. We further anticipate that suppressing both radiative and non-radiative decay rates traps the energy within the molecule instead of re-emitting, thereby possessing possible solutions for programmable emissions in future photonic technologies.

Methodology

Analytical framework

To establish a quantitative physical picture of the toroidal nanoantenna (TNA) platform, we approximate the structure by its dominant bright quasinormal mode (QNM), described by annihilation and creation operators a and a^\dagger , with resonance frequency ω_c . As an open and dissipative plasmonic mode, this QNM is characterized by a total linewidth $\kappa = \kappa_{\text{rad}} + \kappa_{\text{nr}}$, where κ_{rad} denotes radiative leakage into free space and κ_{nr} accounts for non-radiative ohmic dissipation in the metal. A two-level QE, with lowering and raising operators σ and σ^\dagger , transition frequency ω_e , and dipole moment $\boldsymbol{\mu} = \mu \hat{\mathbf{e}}$, is placed at position \mathbf{r}_e . The radiative environment is represented by a continuum of free-space modes $\{b_k\}$, while absorptive loss channels are described by a continuum of bath modes $\{c_q\}$. The use of QNMs and their normalization for open nanophotonic resonators follows established treatments for lossy and leaky systems [58,59].

Within the weak-drive, linear-response regime and under the rotating-wave approximation, the Hamiltonian can be written as

$$\begin{aligned} \frac{H}{\hbar} = & \omega_c a^\dagger a + \omega_e \sigma^\dagger \sigma + (g a \sigma^\dagger + \text{h.c.}) + \sum_k \omega_k b_k^\dagger b_k + \sum_q \omega_q c_q^\dagger c_q \\ & + \sum_k (\eta_k a^\dagger b_k + \text{h.c.}) + \sum_q (\eta_q a^\dagger c_q + \text{h.c.}). \end{aligned} \quad (2)$$

The QE–mode coupling strength is determined by the local QNM field profile,

$$g = \frac{\boldsymbol{\mu} \cdot \mathbf{E}_c(\mathbf{r}_e)}{\hbar} \sqrt{\frac{\hbar \omega_c}{2 \epsilon_0 U_c}}, U_c \propto V_{\text{eff}}, \quad (3)$$

so that

$$g^2 \propto \frac{\mu^2}{V_{\text{eff}}} |\hat{\mathbf{e}} \cdot \mathbf{E}_c(\mathbf{r}_e)|^2. \quad (4)$$

Here, $\mathbf{E}_c(\mathbf{r})$ is the properly normalized QNM field, U_c is the QNM normalization energy, and V_{eff} is the effective mode volume at the emitter position [59,60]. This form makes explicit that strong coupling to the toroidal mode is promoted by both intense local field confinement and small effective modal volume.

The spontaneous-emission rate of the emitter in an inhomogeneous electromagnetic environment is governed by the imaginary part of the Green tensor G_{ij} , according to

$$\gamma_{\text{tot}}(\omega) = \frac{2\omega^2}{\hbar\epsilon_0 c^2} \mu_i \mu_j \text{Im} G_{ij}(\mathbf{r}_e, \mathbf{r}_e; \omega). \quad (5)$$

Near a single dominant bright QNM, the Green tensor assumes a Lorentzian spectral form,

$$\text{Im} G(\mathbf{r}_e, \mathbf{r}_e; \omega) \simeq \frac{A(\mathbf{r}_e) \left(\frac{\kappa}{2}\right)}{(\omega - \omega_c)^2 + (\kappa/2)^2}, \quad A(\mathbf{r}_e) \propto \frac{|\hat{\mathbf{e}} \cdot \mathbf{E}_c(\mathbf{r}_e)|^2}{V_{\text{eff}}}. \quad (6)$$

At resonance ($\omega = \omega_c$), this yields the scaling

$$\gamma_{\text{tot}}^{(\text{res})} \propto \frac{\mu^2}{\hbar^2} \frac{1}{V_{\text{eff}}} \frac{1}{\kappa}, \quad (7)$$

which highlights the central design principle of the TNA platform: maximizing the emission response requires simultaneously reducing the effective mode volume and maintaining a sufficiently narrow bright-mode linewidth.

This interpretation is consistent with the Purcell picture,

$$F_P \equiv \frac{\gamma_{\text{tot}}}{\gamma_0} = \frac{3}{4\pi^2} \left(\frac{\lambda}{n}\right)^3 \frac{Q}{V_{\text{eff}}}, \quad Q \equiv \frac{\omega_c}{\kappa}, \quad (8)$$

which we use here as an instructive scaling relation. Although this canonical form is exact only in the high- Q , Hermitian limit, its QNM generalization remains a useful framework for interpreting emission enhancement in lossy plasmonic resonators.

Because the modal energy can decay through both radiative and ohmic channels, the total spontaneous-emission rate can be partitioned as

$$\gamma_{\text{rad}}^{(\text{res})} = \beta \gamma_{\text{tot}}^{(\text{res})}, \quad \gamma_{\text{nr}}^{(\text{res})} = (1 - \beta) \gamma_{\text{tot}}^{(\text{res})}, \quad \beta = \frac{\kappa_{\text{rad}}}{\kappa_{\text{rad}} + \kappa_{\text{nr}}}. \quad (9)$$

Accordingly, the radiative Purcell factor becomes

$$F_{\text{rad}} = \beta F_P = \beta \frac{3}{4\pi^2} \left(\frac{\lambda}{n}\right)^3 \frac{Q}{V_{\text{eff}}}. \quad (10)$$

This expression makes clear that strong radiative-rate enhancement requires not only subwavelength confinement and favorable modal quality, but also an efficient radiative branching ratio, so that energy coupled into the bright toroidal mode is preferentially emitted rather than dissipated ohmically.

To account for Fano interference, we introduce a narrow discrete resonance with annihilation operator d , resonance frequency ω_0 , and intrinsic linewidth Γ , coupled to the bright QNM with interaction strength J . The additional Hamiltonian term is

$$\frac{H_{\text{narrow}}}{\hbar} = \omega_0 d^\dagger d + (Ja^\dagger d + \text{h. c.}). \quad (11)$$

Under this single-mode dressed-state picture, the effective cavity susceptibility takes the form

$$\chi_c(\omega) = \frac{1}{\omega - \omega_c + i\kappa/2 - \frac{|J|^2}{\omega - \omega_0 + i\Gamma/2}}, \quad (12)$$

showing that the broad bright toroidal mode interferes with a narrow discrete pathway. This interference gives rise to the characteristic asymmetric Fano line shape and, under appropriate coupling and detuning conditions, to sharp transparency minima in the decay spectrum.

In the present system, the quantum objects (QOs) are modeled as dielectric nano-inclusions with narrow Lorentzian resonances. For inclusion volumes $V_i \ll \lambda^3$ and to leading order in the dielectric perturbation $\Delta\epsilon_i(\omega)$, the Lippmann–Schwinger (Dyson) equation yields a first-order correction to the toroid-only Green tensor [61,62],

$$G(\mathbf{r}, \mathbf{r}'; \omega) \simeq G^{(T)}(\mathbf{r}, \mathbf{r}'; \omega) + k_0^2 \sum_i \Delta\epsilon_i V_i G^{(T)}(\mathbf{r}, \mathbf{r}_i; \omega) G^{(T)}(\mathbf{r}_i, \mathbf{r}'; \omega), \quad (13)$$

where $G^{(T)}$ denotes the Green tensor of the isolated toroidal nanoantenna. Within this perturbative picture, the smooth toroidal local density of states (LDOS) interferes with the narrow Lorentzian pole introduced by the QO, producing a Fano-type line shape in both the radiative and non-radiative channels,

$$\frac{\gamma_{r,w\text{QO}}}{\gamma_0} \propto \frac{(\epsilon + q)^2}{1 + \epsilon^2}, \quad (14)$$

with

$$\epsilon = \frac{\omega - \omega_{\text{QO}} - \Delta(\omega)}{\Gamma_{\text{QO}}/2}. \quad (15)$$

Here, q is determined by the complex overlap of the toroidal Green tensor pathways, while $\Delta(\omega)$ represents the real part of the self-energy shift. In the presence of two or more detuned QOs, Eq. (13) naturally generates additional interference terms associated with multiple narrow perturbative pathways embedded within the same toroidal electromagnetic background. In this work, these terms are interpreted as classical or semiclassical interference among several discrete resonant channels, rather than as signatures of many-body quantum correlations.

Numerical methodology

Full-wave simulations were performed using a three-dimensional finite-difference time-domain (FDTD) solver (Ansys Lumerical FDTD Solutions) to solve Maxwell's curl equations for the hybrid QE-TNA-QO system. Spatial and temporal discretization were chosen to satisfy the Courant stability criterion, and perfectly matched layer (PML) boundary conditions were employed in all directions to reproduce open-system behavior.

The optical response of the QOs was modeled using a Lorentzian dielectric function of the form

$$\varepsilon(\omega) = \varepsilon_\infty + \frac{f\omega_0^2}{\omega_0^2 - \omega^2 - i\gamma\omega}, \quad (16)$$

where ε_∞ is the background permittivity, f is the Lorentz oscillator strength, ω_0 is the resonance frequency, and γ is the Lorentzian linewidth. Unless otherwise stated, each QO was taken as a spherical dielectric inclusion with radius 20 nm, oscillator strength 0.2, and linewidth on the order of 10^{10} rad/s, chosen to represent a narrow molecular-like transition. The silver TNA was described using the experimental optical constants reported by Johnson and Christy [63]. The toroid geometry is defined by a major radius R and a cross-sectional radius α .

The QE was modeled as an electric point dipole emitter operating near 850 nm for the aspect-ratio configuration $AR = 0.2$. For other geometries, the emitter wavelength was adjusted to probe the corresponding resonance condition of the TNA. To ensure numerical convergence in the strongly confined near-field region, a fine nonuniform mesh was employed, with local cell sizes ranging from approximately $\lambda/2600$ to $\lambda/600$, depending on the emitter-antenna separation and the associated near-field gradients.

The free-space spontaneous emission rate is given by

$$\gamma_0 = \frac{\omega^3 |\mathbf{p}|^2}{3\pi\varepsilon_0 \hbar c^3}, \quad (17)$$

where ω is the angular frequency and \mathbf{p} is the dipole moment. In the presence of the TNA-QO environment, the radiative decay rate was extracted from far-field power monitors according to

$$\gamma_{\text{rad}} = \frac{P_{\text{rad}}}{P_0} \gamma_0, \quad (18)$$

where P_{rad} is the radiated power collected in the far field and P_0 is the power emitted by the same dipole in free space. The total decay rate was obtained from the total power emitted into the simulation domain,

$$\gamma_{\text{tot}} = \frac{P_{\text{tot}}}{P_0} \gamma_0, \quad (19)$$

with P_{tot} evaluated from the total electromagnetic power flux through a closed surface surrounding the dipole and the hybrid nanostructure. The non-radiative decay rate then follows directly as

$$\gamma_{\text{nr}} = \gamma_{\text{tot}} - \gamma_{\text{rad}}. \quad (20)$$

Specifically, the total emitted power is calculated from the surface integral of the Poynting vector over a closed near-field surface S ,

$$P_{\text{tot}} = \oint_S \mathbf{S} \cdot d\mathbf{A}, \quad (21)$$

while the radiated power is obtained from an analogous integration over a far-field monitor surface S_{far} ,

$$P_{\text{rad}} = \oint_{S_{\text{far}}} \mathbf{S} \cdot d\mathbf{A}. \quad (22)$$

This separation allows direct discrimination between power emitted to the far field and power dissipated non-radiatively through absorption or near-field energy transfer processes.

To parameterize the distance dependence of the QE-TNA interaction, the decay-rate variation with emitter–antenna separation x was fitted using an empirical exponential form,

$$y_i(x) = \exp(a + bx + cx^2), \quad (23)$$

where the fitting coefficients were obtained separately for the radiative and non-radiative channels. For the radiative decay rate, the coefficients are $a = 8.40839$, $b = -0.16056$, and $c = 0.00162$, whereas for the non-radiative decay rate they are $a = 7.52683$, $b = -0.20485$, and $c = 0.00243$. These fits are used only to parameterize the simulated distance dependence and do not enter the electromagnetic solver itself.

Acknowledgments

E.O.P. acknowledges financial support from the Scientific and Technological Research Council of Türkiye (TÜBİTAK) through Grant No. 222N308 within the CHIST-ERA program and BILKENT University- TUBITAK BILGEM Consultancy Call for Research (BIL2). Additional support was provided by the Turkish Academy of Sciences Outstanding Young Scientists Awards (TUBA-GEBİP) 2025.

Author Contributions

A.G. performed the numerical simulations, carried out the calculations, and extracted the raw data underlying the reported results. A.G. also contributed to the preparation of the manuscript. E.O.P. conceived the research idea, supervised the project, and led the preparation of the manuscript, including the development of the final figures and the main text. All authors discussed the results and contributed to the final version of the manuscript.

Competing interests

The authors declare no competing interests.

Data availability

All data necessary to evaluate the results presented in this work are included within the paper. Additional datasets supporting the findings of this study are available from the corresponding author upon reasonable request.

References

- [1] Y. Wy, H. Jung, J. W. Hong, and S. W. Han, “Exploiting Plasmonic Hot Spots in Au-Based Nanostructures for Sensing and Photocatalysis,” *Acc. Chem. Res.* **55**, 831 (2022).
- [2] S. A. Maier, M. L. Brongersma, P. G. Kik, S. Meltzer, A. A. G. Requicha, and H. A. Atwater, “Plasmonics—A Route to Nanoscale Optical Devices,” *Adv. Mater* **13**, 1501 (2001).
- [3] S. A. Maier and others, “*Plasmonics: Fundamentals and Applications*,” Vol. 1 (Springer, 2007).
- [4] K. Kneipp, Y. Wang, H. Kneipp, L. T. Perelman, I. Itzkan, R. R. Dasari, and M. S. Feld, “Single Molecule Detection Using Surface-Enhanced Raman Scattering (SERS),” *Phys. Rev. Lett.* **78**, 1667 (1997).
- [5] E. Ozbay, “Plasmonics: Merging photonics and electronics at nanoscale dimensions,” *Science* (1979) **311**, 189 (2006).
- [6] A. Gulucu and E. O. Polat, “Optically Switchable Fluorescence Enhancement at Critical Interparticle Distances,” *Adv. Theory Simul.* **8**, e01134 (2025).
- [7] R. Sharma, N. K. Pathak, and R. P. Sharma, “Computational Study of Plasmon Interaction in Organic Media: a Comparison Between Analytical and Numerical Model for Dimer,” *Plasmonics* **13**, 1775 (2018).
- [8] Y. F. Xiao, Y. C. Liu, B. B. Li, Y. L. Chen, Y. Li, and Q. Gong, “Strongly enhanced light-matter interaction in a hybrid photonic-plasmonic resonator,” *Phys. Rev. A* **85**, 031805 (2012).
- [9] J. Cao, T. Sun, and K. T. V. Grattan, “Gold nanorod-based localized surface plasmon resonance biosensors: A review,” *Sens. Actuators. B: Chem.* **195**, 332 (2014).
- [10] T. Kaelberer, V. A. Fedotov, N. Papasimakis, D. P. Tsai, and N. I. Zheludev, “Toroidal Dipolar Response in a Metamaterial,” *Science* (1979) **330**, 1510 (2010).
- [11] N. Papasimakis, V. A. Fedotov, V. Savinov, T. A. Raybould, and N. I. Zheludev, “Electromagnetic toroidal excitations in matter and free space,” *Nat. Mater* **15**, 263 (2016).
- [12] A. Mary, A. Dereux, and T. L. Ferrell, “Localized surface plasmons on a torus in the nonretarded approximation,” *Phys. Rev. B Condens. Matter Mater. Phys.* **72**, 155426 (2005).
- [13] T. Warnakula, S. D. Gunapala, M. I. Stockman, and M. Premaratne, “Broken poloidal symmetry and plasmonic eigenmodes on a torus,” *Phys. Rev. B* **101**, 115426 (2020).
- [14] T. V. Teperik and A. Degiron, “Numerical analysis of an optical toroidal antenna coupled to a dipolar emitter,” *Phys. Rev. B Condens. Matter Mater. Phys.* **83**, 245408 (2011).
- [15] C. M. Dutta, T. A. Ali, D. W. Brandl, T. H. Park, and P. Nordlander, “Plasmonic properties of a metallic torus,” *J. Chem. Phys.* **129**, (2008).
- [16] J. Aizpurua, P. Hanarp, D. S. Sutherland, M. Käll, G. W. Bryant, and F. J. García de Abajo, “Optical Properties of Gold Nanorings,” *Phys. Rev. Lett.* **90**, 4 (2003).
- [17] H. E. M. Purcell, “*Spontaneous Emission Probabilities at Radio Frequencies*,” in *Confined Electrons and Photons: New Physics and Applications* (Springer, 1995).
- [18] K. V. Garapati, M. Salhi, S. Kouchekian, G. Siopsis, and A. Passian, “Poloidal and toroidal plasmons and fields of multilayer nanorings,” *Phys. Rev. B* **95**, 165422 (2017).

- [19] M. F. Limonov, M. V. Rybin, A. N. Poddubny, and Y. S. Kivshar, “Fano resonances in photonics,” *Nat. Photonics* **11**, 543 (2017).
- [20] U. Fano, “Effects of Configuration Interaction on Intensities and Phase Shifts,” *Phys. Rev.* **124**, 1866 (1961).
- [21] M. Pelton, S. D. Storm, and H. Leng, “Strong coupling of emitters to single plasmonic nanoparticles: exciton-induced transparency and Rabi splitting,” *Nanoscale* **11**, 14540 (2019).
- [22] N. Liu, L. Langguth, T. Weiss, J. Kästel, M. Fleischhauer, T. Pfau, and H. Giessen, “Plasmonic analogue of electromagnetically induced transparency at the Drude damping limit,” *Nat. Mater* **8**, 758 (2009).
- [23] H. Leng, B. Szychowski, M. C. Daniel, and M. Pelton, “Strong coupling and induced transparency at room temperature with single quantum dots and gap plasmons,” *Nat. Commun.* **9**, 1 (2018).
- [24] M. Pelton, S. K. Gray, and X. Wu, “Quantum-dot-induced transparency in a nanoscale plasmonic resonator,” *Opt. Express* **18**, 23633 (2010).
- [25] S. Zhang, D. A. Genov, Y. Wang, M. Liu, and X. Zhang, “Plasmon-induced transparency in metamaterials,” *Phys. Rev. Lett.* **101**, 047401 (2008).
- [26] Y. Zheng et al., “Fano Resonance in Single-Molecule Junctions,” *Angew. Chem. - Int. Ed.* **61**, 10097 (2022).
- [27] A. E. Miroshnichenko, S. Flach, and Y. S. Kivshar, “Fano resonances in nanoscale structures,” *Rev. Mod. Phys.* **82**, 2257 (2010).
- [28] B. Luk’Yanchuk, N. I. Zheludev, S. A. Maier, N. J. Halas, P. Nordlander, H. Giessen, and C. T. Chong, “The Fano resonance in plasmonic nanostructures and metamaterials,” *Nat. Mater* **9**, 707 (2010).
- [29] Q. Shi, Z. Yu, Y. Liu, H. Gong, H. Yin, W. Zhang, J. Liu, and Y. Peng, “Plasmonics properties of nano-torus: An FEM method,” *Opt. Commun.* **285**, 4542 (2012).
- [30] M. Pelton, S. K. Gray, and X. Wu, “Quantum-dot-induced transparency in a nanoscale plasmonic resonator,” *Opt. Express* **18**, 23633 (2010).
- [31] H. Leng, B. Szychowski, M. C. Daniel, and M. Pelton, “Strong coupling and induced transparency at room temperature with single quantum dots and gap plasmons,” *Nat. Commun.* **9**, 4012 (2018).
- [32] J. Yan, C. Ma, P. Liu, C. Wang, and G. Yang, “Generating scattering dark states through the Fano interference between excitons and an individual silicon nanogroove,” *Light Sci. Appl.* **6**, e16197 (2016).
- [33] R. A. Shah, N. F. Scherer, M. Pelton, and S. K. Gray, “Ultrafast reversal of a Fano resonance in a plasmon-exciton system,” *Phys. Rev. B* **88**, 075411 (2013).
- [34] A. Hassanfiroozi, P. S. Huang, S. H. Huang, K. I. Lin, Y. T. Lin, C. F. Chien, Y. Shi, W. J. Lee, and P. C. Wu, “A Toroidal-Fano-Resonant Metasurface with Optimal Cross-Polarization Efficiency and Switchable Nonlinearity in the Near-Infrared,” *Adv. Opt. Mater* **9**, 2101007 (2021).

- [35] Q. Mi, T. Sang, Y. Pei, C. Yang, S. Li, Y. Wang, and B. Ma, “High-quality-factor dual-band Fano resonances induced by dual bound states in the continuum using a planar nanohole slab,” *Nanoscale Res. Lett.* **16**, 150 (2021).
- [36] N. Papasimakis, V. A. Fedotov, N. I. Zheludev, and S. L. Prosvirnin, “Metamaterial Analog of Electromagnetically Induced Transparency,” *Phys. Rev. Lett.* **101**, 253903 (2008).
- [37] S. Zhang, D. A. Genov, Y. Wang, M. Liu, and X. Zhang, “Plasmon-Induced Transparency in Metamaterials,” *Phys. Rev. Lett.* **101**, 047401 (2008).
- [38] E. O. Polat, Z. Artvin, Y. Şaki, A. Bek, and R. Sahin, “Continuous and Reversible Electrical Tuning of Fluorescent Decay Rate via Fano Resonance,” *ArXiv Preprint 2412.20199* (2024).
- [39] D. A. B. Miller, D. S. Chemla, T. C. Damen, A. C. Gossard, W. Wiegmann, T. H. Wood, and C. A. Burrus, “Band-Edge Electroabsorption in Quantum Well Structures: The Quantum-Confined Stark Effect,” *Phys. Rev. Lett.* **53**, 2173 (1984).
- [40] Y. Miao, R. C. Boutelle, A. Blake, V. Chandrasekaran, C. J. Sheehan, J. Hollingsworth, D. Neuhauser, and S. Weiss, “Super-resolution Imaging of Plasmonic Near-Fields: Overcoming Emitter Mislocalizations,” *J. Phys. Chem. Lett.* **13**, 4520 (2022).
- [41] C. Lee, B. Lawrie, R. Pooser, K. G. Lee, C. Rockstuhl, and M. Tame, “Quantum Plasmonic Sensors,” *Chem. Rev.* **121**, 4743 (2021).
- [42] W. Bogaerts, D. Pérez, J. Capmany, D. A. B. Miller, J. Poon, D. Englund, F. Morichetti, and A. Melloni, “Programmable photonic circuits,” *Nature* **586**, 207 (2020).
- [43] X. Duan, S. Kamin, and N. Liu, “Dynamic plasmonic colour display,” *Nat. Commun.* **8**, 1 (2017).
- [44] L. Novotny and B. Hecht, “*Principles of Nano-Optics*,” (Cambridge University Press, 2012).
- [45] R. Carminati, J. J. Greffet, C. Henkel, and J. M. Vigoureux, “Radiative and non-radiative decay of a single molecule close to a metallic nanoparticle,” *Opt. Commun.* **261**, 368 (2006).
- [46] G. W. Wen, J. Y. Lin, H. X. Jiang, and Z. Chen, “Quantum-confined Stark effects in semiconductor quantum dots,” *Phys. Rev. B* **52**, 5913 (1995).
- [47] I. Niehues, E. D. S. Nysten, R. Schmidt, M. Weiß, and D. Wigger, “Excitons in quantum technologies: The role of strain engineering,” *MRS Bull.* **49**, 958 (2024).
- [48] H. Bahmani Jalali, L. De Trizio, L. Manna, and F. Di Stasio, “Indium arsenide quantum dots: an alternative to lead-based infrared emitting nanomaterials,” *Chem. Soc. Rev.* **51**, 9861 (2022).
- [49] S. Castelletto, F. A. Inam, S. I. Sato, and A. Boretti, “Hexagonal boron nitride: a review of the emerging material platform for single-photon sources and the spin–photon interface,” *Beilstein J. Nanotechnol.* **11**, 740 (2020).
- [50] D. Liu, F. Kaiser, V. Bushmakina, E. Hesselmeier, T. Steidl, T. Ohshima, N. T. Son, J. Ul-Hassan, Ö. O. Soykal, and J. Wrachtrup, “The silicon vacancy centers in SiC: determination of intrinsic spin dynamics for integrated quantum photonics,” *Npj Quantum Inf.* **10**, 72 (2024).
- [51] M. Liu et al., “Multifunctional metasurfaces enabled by simultaneous and independent control of phase and amplitude for orthogonal polarization states,” *Light Sci. Appl.* **10**, 1 (2021).
- [52] T. Roesel, A. Dahlin, M. Piliarik, L. W. Fitzpatrick, and B. Špačková, “Label-free single-molecule optical detection,” *Npj Biosensing* **2025 2:1** **2**, 1 (2025).

- [53] S. W. Chong, Y. Shen, S. Palomba, and D. Vigolo, “Nanofluidic Lab-On-A-Chip Systems for Biosensing in Healthcare,” *Small* **21**, 2407478 (2025).
- [54] N. A. Salama, S. M. Alexeree, S. S. A. Obayya, and M. A. Swillam, “Silicon-based double fano resonances photonic integrated gas sensor,” *Sci. Rep.* **14**, (2024).
- [55] H. J. Chen, “Multiple-Fano-resonance-induced fast and slow light in the hybrid nanomechanical-resonator system,” *Phys. Rev. A* **104**, 013708 (2021).
- [56] Y. Huo, T. Jia, T. Ning, C. Tan, S. Jiang, C. Yang, Y. Jiao, and B. Man, “A low lasing threshold and widely tunable spaser based on two dark surface plasmons,” *Sci. Rep.* **7**, 1 (2017).
- [57] N. K. Emani, T. F. Chung, A. V. Kildishev, V. M. Shalaev, Y. P. Chen, and A. Boltasseva, “Electrical modulation of fano resonance in plasmonic nanostructures using graphene,” *Nano Lett.* **14**, 78 (2014).
- [58] C. Sauvan, J. P. Hugonin, I. S. Maksymov, and P. Lalanne, “Theory of the Spontaneous Optical Emission of Nanosize Photonic and Plasmon Resonators,” *Phys. Rev. Lett.* **110**, 237401 (2013).
- [59] P. T. Kristensen, R. C. Ge, and S. Hughes, “Normalization of quasinormal modes in leaky optical cavities and plasmonic resonators,” *Phys. Rev. A* **92**, 053810 (2015).
- [60] E. A. Muljarov and W. Langbein, “Exact mode volume and Purcell factor of open optical systems,” *Phys. Rev. B* **94**, 235438 (2016).
- [61] W. Cho. Chew, “*Waves and fields in inhomogeneous media*,” (John Wiley & Sons, 1999).
- [62] O. J. F. Martin, C. Girard, and A. Dereux, “Generalized Field Propagator for Electromagnetic Scattering and Light Confinement,” *Phys. Rev. Lett.* **74**, 526 (1995).
- [63] P. B. Johnson and R. W. Christy, “Optical Constants of the Noble Metals,” *Phys. Rev. B* **6**, 4370 (1972).

Supplementary Information for
Programmable Switching of Molecular Transitions via Plasmonic Toroidal
Nanoantennae

Arda Gulucu^{1,2} and Emre Ozan Polat^{1,2,*}

¹*Department of Physics, Bilkent University, 06800, Ankara, Turkey*

²*UNAM – National Nanotechnology Research Center and Institute of Materials Science and Nanotechnology, Bilkent University, 06800, Ankara, Turkey*

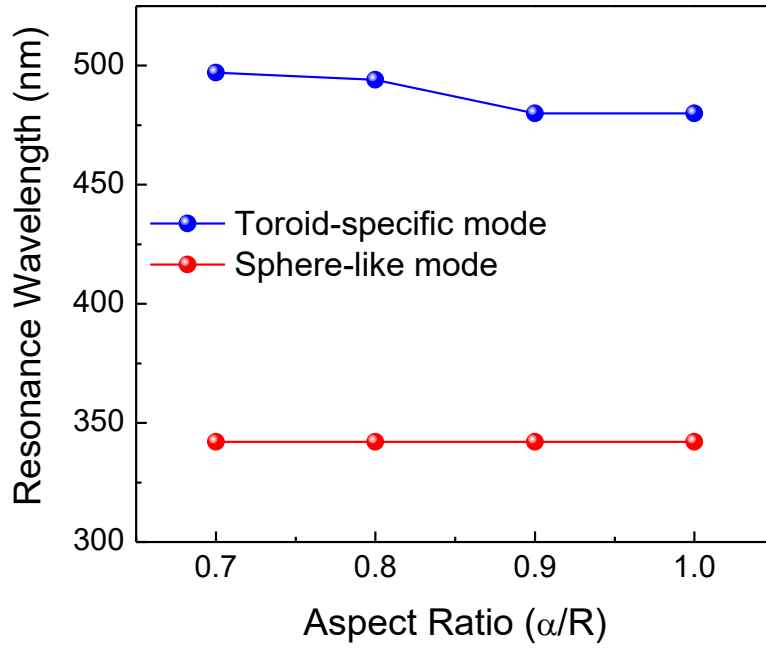
**Corresponding author: emre.polat@bilkent.edu.tr*

The supplementary figures provide additional numerical results supporting the plasmonic modal crossover from a toroid-specific branch to a sphere-like branch discussed in the main text. They track the evolution of the resonance wavelengths, as well as the corresponding radiative and nonradiative decay channels, across the high-aspect-ratio regime.

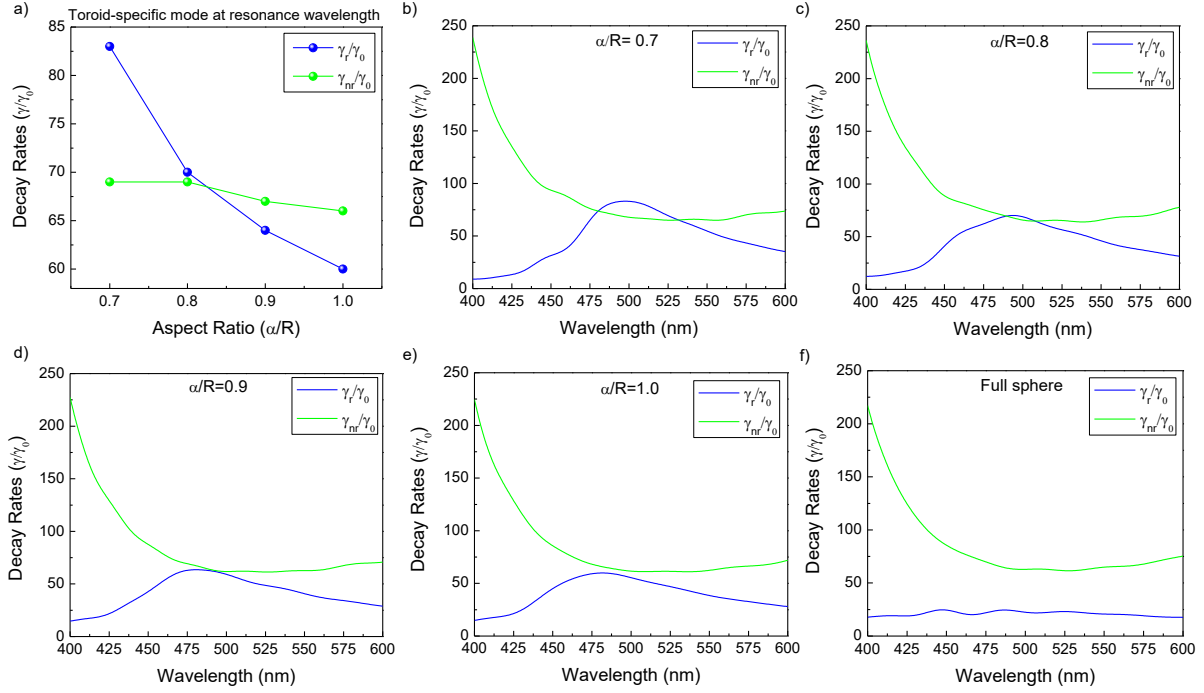
Supplementary Figure S1. Dependence of the resonance wavelength on aspect ratio for the toroid-specific and sphere-like plasmon branches in the range $\alpha/R = 0.7-1.0$.

Supplementary Figure S2. Radiative (γ_r/γ_0) and nonradiative (γ_{nr}/γ_0) decay rates of the toroid-specific plasmon branch.

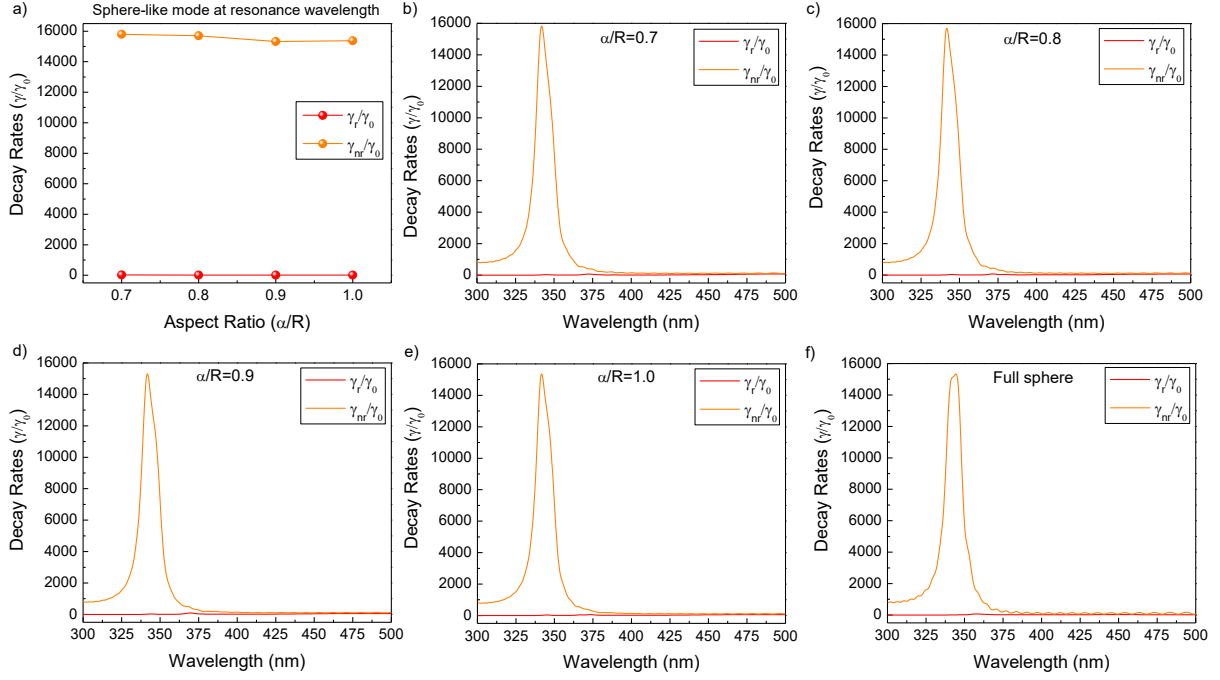
Supplementary Figure S3. Radiative and nonradiative decay rates of the sphere-like plasmon branch supported by the toroidal nanoantenna.



Supplementary Figure S1. Dependence of the resonance wavelength on aspect ratio for the toroid-specific and sphere-like plasmon branches in the range $\alpha/R = 0.7-1.0$. The toroid-specific branch remains at longer wavelengths and exhibits a slight blueshift with increasing aspect ratio, whereas the sphere-like branch stays nearly fixed at ~ 342 nm. The persistence of the short-wavelength branch within the toroidal geometry, together with its weak spectral dispersion, supports its assignment as a sphere-like mode rather than a topology-dependent toroid mode.



Supplementary Figure S2. Radiative (γ_r/γ_0) and nonradiative (γ_{nr}/γ_0) decay rates of the toroid-specific plasmon branch. (a) At the toroid resonance wavelength, both decay channels change smoothly with increasing aspect ratio (α/R), indicating the absence of any pronounced nonradiative-loss enhancement. **(b-e)** Spectral decay-rate profiles for $\alpha/R = 0.7$ -1.0 confirm that the toroid branch persists as a broad resonance in the visible range, with balanced radiative and nonradiative contributions. **(f)** For comparison, the decay-rate spectrum of a reference silver nanosphere ($R = 60$ nm) is included, emphasizing the distinct behavior



Supplementary Figure S3. Radiative and nonradiative decay rates of the sphere-like plasmon branch supported by the toroidal nanoantenna. (a) At resonance, the decay rates for $\alpha/R = 0.7\text{--}1.0$ show that this short-wavelength branch is overwhelmingly nonradiative, with extremely large γ_{nr}/γ_0 and negligible γ_r/γ_0 . (b–e) The spectral profiles reveal a narrow resonance near ~ 342 nm that remains nearly purely nonradiative across all aspect ratios considered. (f) The decay-rate spectrum of a reference silver nanosphere is shown for comparison, confirming the sphere-like character of this branch.